Surface Science 712 (2021) 121888

Contents lists available at ScienceDirect

Surface Science

journal homepage: www.elsevier.com/locate/susc

Tailoring the redox capabilities of organic ligands for metal-ligand coordination with vanadium single-sites

Tobias W. Morris [a,†], David L. Wisman [a,b,†], Nassem U. Din [c], Duy Le [c], Talat S. Rahman [c], Steven L. Tait [a,*]

[a] Department of Chemistry, Indiana University, Bloomington, Indiana, USA
[b] NAVSEA Crane, Crane, Indiana, USA
[c] Department of Physics, University of Central Florida, Orlando, Florida, USA

ARTICLE INFO

Keywords:
Metal-organic coordination
On-surface redox assembly
Scanning tunneling microscopy
Density functional calculations
X-ray photoelectron spectroscopy
Redox-active ligands
Charge transfer
Metals

ABSTRACT

The creation of single-site metal centers (SSMCs) through the formation of metal-organic coordination networks is an area of interest due to the proven ability of SSMCs to improve selectivity for heterogeneous catalysts. In order to better understand the reactivity potential for the SSMCs it is necessary to study the ligand-metal interaction in the metal-organic coordination networks. In the work reported here, we demonstrate the ability to tune the oxidation state of vanadium from II to IV through the tailoring of redox-active ligands. Using the N-heterocyclic ligands of bipyrimidine (**BP**), bispyrimidinyltetrazine (**BMTZ**), and biimidazole (**BIM**) complexed with metallic V, we have shown that the oxidation state of the V metal centers can be tuned to V(II) for **BP**, V(III) for **BMTZ**, and V(IV) for **BIM**. These redox-active ligands provide similar coordination environments when complexed into one dimensional chains but result in different oxidation states for the single-site metal center.

1. Introduction

Catalytic processes represent a vital and growing portion of the industrial processes responsible for the global economy and as such the continued development of cheaper, more efficient and selective catalysts are essential for the continued growth of these processes. One method for increasing the catalytic efficiency is through the use of single atom catalysts (SACs). SACs have been shown to have increased active-site density and higher recyclability compared to traditional metal nanoparticles [1–5] and have demonstrated enhanced selectivity and reactivity in a variety of reactions compared to traditional bulk catalysts with the use of metals such as Pt and Pd [6–8].

Our group has developed methods of forming single-site metal centers through the use of a redox-active organic ligand to form metal-organic coordination networks (MOCNs) [9–13]. MOCNs allow for higher loading of the SAC, readily accessible tuning of the metal oxidation state, and provide uniformity in the SACs of the systems studied. Analogous to molecular homogeneous catalysts, MOCNs allow for careful tuning of the electronic and steric properties of the metal active site through rational ligand choice. The ability to deposit a zero-valent atomic metal allows enhanced oxidation state control through the degree of redox activity in the co-deposited organic ligand as well as the presence of reducible protons, making the ligand an essential part of the overall system.

Nitrogen heterocycles composed entirely of imine functionality broaden this potential for redox chemistry considerably because every sp^2 nitrogen lowers the energy of the ring π^* orbital and thus increases its ease of reduction. N-heterocyclic ligands with nitrogen lone pairs diametrically opposed, have the potential for chain formation through surface assembled complexes with equimolar stoichiometry. By controlling the electronic structure, particularly the oxidation state, of the active metal site, specific chemical transformations can be targeted [14–16].

In the work reported here, we demonstrate the ability to tune the oxidation state of vanadium from II to IV through the tailoring of the redox-active ligands. We examine three such redox-active ligands (Scheme 1), which provide similar coordination environments when assembled into one dimensional chains but result in different oxidation states of the single-site metal center upon complexation. All three ligands are two-fold symmetric, comprised of four nitrogen-donors

* Corresponding author.
E-mail address: tait@indiana.edu (S.L. Tait).
† These authors contributed equally to this work.

https://doi.org/10.1016/j.susc.2021.121888
Received 27 January 2021; Received in revised form 21 May 2021; Accepted 31 May 2021
Available online 5 June 2021

providing diametric binding sites for incoming metals to give repeating units of four-coordinate square-planar metal sites, a geometry explored in our previous work [9–12]. While providing assemblies of similar structure, the three ligands differ drastically in terms of their potential for oxidizing an incoming zero-valent metal. In each experiment, zero-valent metal is deposited to the surface by vapor deposition from a pure metal rod.

The least oxidizing ligand, bipyrimidine (**BP**), is comprised of two pyrimidine moieties bonded in the 2-position to give a 1,4-azabutadiene and two equivalent binding pockets. The 1,4-azabutadiene unit is an extensively studied ligand functionality which is well-known for its redox-activity [17]. The presence of this functionality is due to the extended π-system of the aromatic scaffold. We propose that this should lead to the storage of two electrons within the ligand backbone resulting in an assembly composed of divalent metal sites. Biimidazole (**BIM**), contains the same redox-active 1,4-azabutadiene functionality expected to allow for two-electron transfer from metal to ligand, but also incorporates two acidic protons. When reacted with zero-valent atomic metal, these acidic protons can lead to irreversible dihydrogen loss (proton reduction) and subsequent metalation [18]. The incorporation of this bi-functionality is expected to allow for access to the tetravalent oxidation state without losing availability of the apical binding site (retention of coordination environment) or necessitating an additional oxidant. We also report new results for bispyrimidinyltetrazine (**BMTZ**), a ligand which has been studied previously in our group and was shown to oxidize an incoming metal by greater than two electrons, resulting in assemblies of trivalent metal centers when reacted with vanadium [10]. As with the closely related dipyridyltetrazine (**DPTZ**), the defining feature of **BMTZ** is the ability for initial two-electron transfer to the low energy π* orbital of the tetrazine linker, but by replacing the pyridyl arms with pyrimidine units the overall scaffold is able to accept another electron from the reducing metal partner.

While rational ligand choice is often the most important consideration, and the primary focus of the work reported here, careful selection of the metal is important for determining the electronic structure of the resulting assemblies and any subsequent reactivity observed. In this work, we focus on the first-row transition metal vanadium. Vanadium serves as an ideal metal for exploring the tunability of these MOCNs due to its ability to exist in multiple oxidation states (II-V) as well as the drastically different reactivity observed between the oxidation states. As an early transition metal, vanadium in its low oxidation states has a propensity to facilitate reductive processes [19] due to its inherent electron richness, whereas vanadium in its high oxidation states has been found to catalyze a number of oxidative transformations [20–26]. These features make vanadium an enticing target for the development of MOCN systems with selectivity controlled through ligand design, highlighting the tunability of these systems

2. Experimental methods

All experiments were conducted in an ultra-high vacuum (UHV) system ($< 5 \times 10^{-10}$ Torr) comprised of three interconnected chambers which allowed physical and chemical measurements to be made free of external contamination during the stages of sample preparation. Local topographical information was obtained from a SPM UHV 750, RHK Technologies scanning probe microscope (SPM) while chemical identification was obtained using a SPECS GmBH dual anode XPS system (electron energy analyzer PHOIBOS 150, XR-50 Mg/Al dual anode X-ray source).

The Au(111) single crystal surface (Princeton Scientific) was prepared by repeated cycles of argon ion sputtering at a sample temperature of 200 C and thermal annealing at temperatures 500 ℃. All molecules were deposited from a quartz crucible from a Knudsen-type evaporator in UHV at temperatures between 120–130 ℃ and surface cleanliness was verified with XPS. The ligands **BIM** (96%, Matrix Scientific) and **BP** (97%, Ambeed) were commercially purchased while the synthesis of **BMTZ** has previously been reported [10]. Vanadium (99.7% pure rod, Goodfellow) was vapor deposited onto the surface using an electron beam evaporator (QUAD-EV-S Mini e-beam Evaporator, Mantis Deposition Ltd.).

All STM images were acquired at room temperature using tunneling currents between 0.1 and 0.5 nA and bias voltages of 0.9 to 1.5 V unless

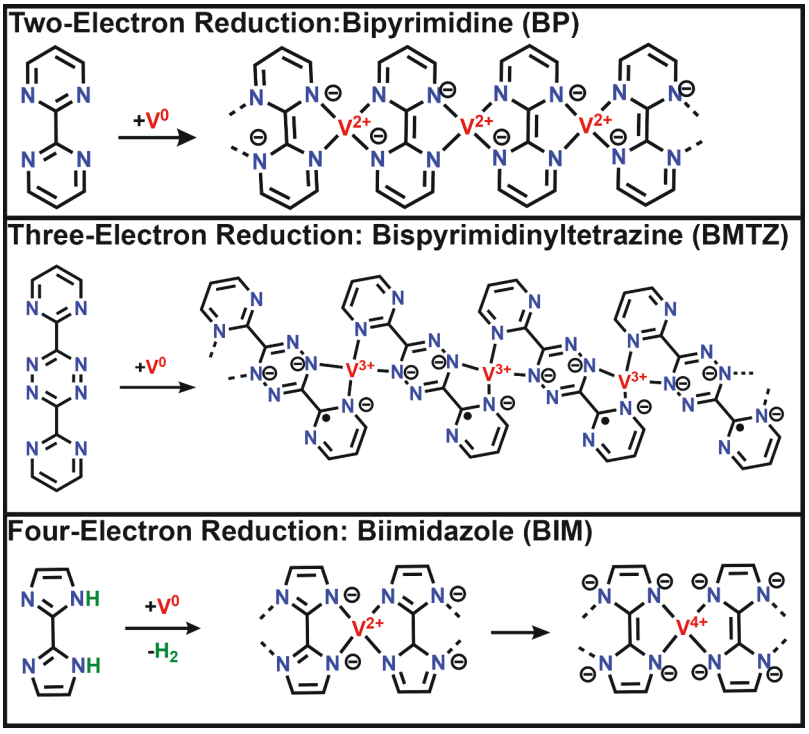

Scheme 1. Proposed metal-organic coordination networks comprised of vanadium complexed with three different nitrogen heterocycle based ligands: Bipyrimidine (**BP**) Bispyrinidinyltetrazine (**BMTZ**), and Biimidazole (**BIM**). These complexes have the potential to tune the oxidation state of vanadium from V(II) to V(IV).

otherwise stated using electrochemically etched tungsten tips [27, 28]. STM images were analyzed using global plane subtractions and/or line-by-line linear flattening with no filtering using WSxM [29], and calibrated using the well-studied structure of terephthalic acid on a Cu (100) surface [30, 31]. All XPS data were calibrated in energy to the Au $4f_{7/2}$ peak (84.0 eV) and normalized to the height of that peak to account for variation in the photon intensity and analyzer sensitivity.

3. Computational methods

Spin-polarized density functional theory (DFT) simulations were performed for gas phase **V-BP** chains and for **V-BP** on an Au(111) surface using the Vienna Ab-initio Simulation Package (VASP) [32] employing the projector-augmented wave (PAW) [33] and plane wave basis set methods. The generalized gradient approximation (GGA) proposed by Perdew, Burke, and Ernzerhof (PBE) [34] together with the DFT-D3 correction [35] were used to describe the exchange-correlation of electrons and to account for van der Waals interaction. The energy cutoff for plane wave expansion was set to 500 eV.

The simulation of the supercell for gas phase calculations consists of two **BP** molecules and two V atoms corresponding to M:**BP** ratio of 1:1. A $3 \times 1 \times 1$mesh is used in performing integration over the Brillouin zone for both gas phase as well as on support calculations, which is sufficient for the convergence of formation energy. For the system consisting of the **BP** ligands and V adatoms on the Au(111) surface, the supercell consists of two V atoms, two **BP** ligands, and a five-layer Au(111) slab, all together, thus having 198 atoms in the supercell. A vacuum layer of about 15 Å was used to minimize unwanted interactions between periodical images. During ionic relaxation, the bottom three Au layers are held fixed at their bulk position. All structures are relaxed until all force components acting on each ion reach a threshold of 0.01 eV/Å.

4. Results and discussion

In the results reported here, V metal was used to explore the redox capabilities of the organic ligands primarily because of its ability to exist in multiple adjacent oxidation states. Additionally, metal-ligand complexes utilizing V metal centers have been widely studied for applications in heterogeneous catalysis [19, 24] while vanadium oxides are also commonly used in homogenous catalysis [26, 36–40]. Fig. 1 shows XP spectra of the V 2*p* region upon complexation with the different organic ligands utilized in this study. As discussed below, these ligands allow the V to adopt oxidation states of V(II), V(III), or V(IV). These are each compared to zero-valent V (top curve of Fig. 1), which is obtained when no ligand is present on the surface. Note that V is vapor deposited to the surface from a pure V rod, so in the absence of an oxidizing ligand, it remains as V(0). Binding energies are referenced in each experiment to the position of the Au 4*f* peak. We also note that the full-width at half-maximum (FWHM) for the first four spectra in Fig. 1 are similar and each consistent with the vanadium having a single predominant oxidation state. The last spectrum, V-BIM, has a larger width indicating more than one V species, which is discussed below.

The relative binding energy positions of the spectra in Fig. 1 clearly indicates a difference in the local chemical state of the V species in these samples. In this work, we will primarily interpret these as oxidation state differences due to variation of the electron acceptor character of the ligands studied. Final state effects, charge transfer between the support surface and the metal center, and other effects could also impact the measured binding energy, however, since the immediate environment around the V center in each case (N atoms from ligands and underlying Au surface) is quite similar, we think it is reasonable to consider the observed differences in the context of oxidation changes in the redox assembly of V with the ligands studied, as has been discussed previously [9–13].

The aromatic core of **BP** allows for a potential of two electrons to be stored in the ligand, making it the least oxidizing of the ligands studied here. The diverging binding pockets shown in Scheme 1 allow for the formation of a square-planar geometry for the V metal upon complexation with **BP**. Upon exposure of V to **BP**, and subsequent annealing to 150 °C, the V $2p_{3/2}$ peak is observed to shift at a higher binding energy (BE) of 513.8 eV when compared to that of metallic V which is observed at 512.9 eV (Fig. 1). This shift to higher BE compared to metallic V is consistent with oxidation of the metal center to a V(II) species, which agrees with our previously reported results for V(II) species in V-**DPTZ** (di-pyridyl-tetrazine) [10, 41]. **DPTZ** contains a central tetrazine ring, which makes it significantly larger than **BP**, but the experiments here demonstrate that the more compact **BP** is capable of comparable oxidizing potential. Due to the smaller size of **BP**, it is noticeably more mobile than **DPTZ**; when **DPTZ** is deposited on the surface without metal, we are able to observe islands of pure **DPTZ** [10], but **BP** does not form similar islands without a coordinating metal to stabilize it.

Nitrogen 1*s* data, shown in Fig. 2 provides additional evidence of the reduction of **BP** before and after complexation with metallic V. Deposition of free ligand **BP** on Au(111) shows a single species of nitrogen

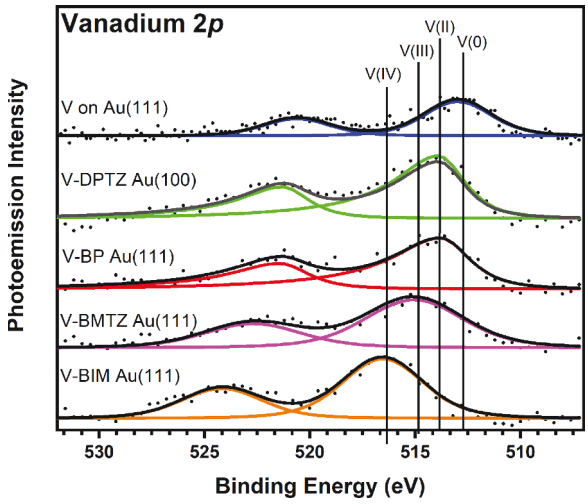

Fig.1. XP spectra of the V 2*p* region showing the shift of V metal upon complexation with different redox-active ligands. The increasing redox ability of the ligands is demonstrated by the sequential shift of the V peak to higher binding energy.

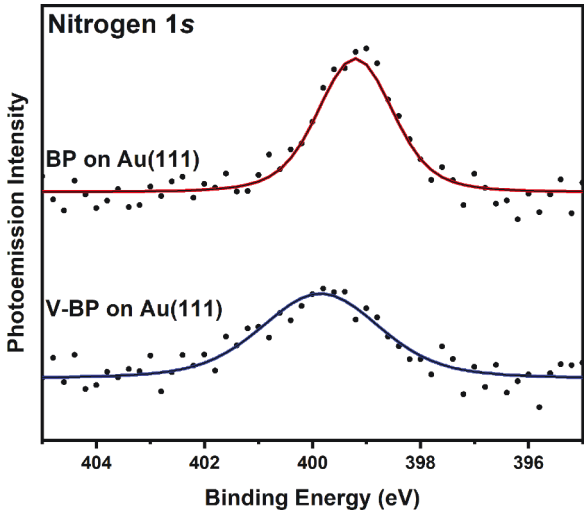

Fig. 2. N 1*s* XP spectra of **BP** and V-**BP** on Au(111) showing the peak shift to higher BE, and an increase in the FWHM is observed following complexation with vanadium. Coverage of **BP** on Au(111) is 1.5 ML and of V-**BP** on Au(111) is 0.5 ML, as determined by XPS.

with a BE of 399.2 eV and a FWHM of 1.6 eV. This measured binding energy value is higher than previous studies looking at a pyrimidine based ligand [10], and is attributed to charge transfer from the ligand to the underlying Au substrate [42].

Upon complexation with V and subsequent annealing at 150 °C the N 1*s* peak shifts to higher BE (399.9 eV) and the FWHM of the N 1*s* peak increases to 2.6 eV (Fig. 2). The increase in the FWHM of the N 1*s* may be due to delocalization of charge across the pyrimidine rings, as reported previously for **BMTZ** [10], or to multiple chemical states of N in this system. The observed shift to higher BE of the N 1*s* peak is indication of charge transfer from V-**BP** to the underlying Au(111) surface. This charge transfer from the ligand to the substrate upon complexation with V is also evident in the DFT model shown in Fig. 3a.

As discussed previously, one advantage of MOCNs is the uniform surface structure that is observed using scanning probe microscopy. Examinations of the surface using STM were not able to provide any insight into the V-**BP** structure, as shown in Fig. 3c. The classic Au(111) herringbone reconstruction is visible in the image suggesting good tip quality, but no structure is observed. XPS measurements of the surface indicate a coverage of 0.5 ML, so the lack of an observed surface structure suggests the V-**BP** complex is mobile at room temperature. We therefore turned to DFT calculations to provide rationale into the mobility of the complex and lack of surface structure. DFT investigations of the orientation of the **BP** molecule shows significant twisting of 32° for the gas-phase V-**BP** complex (Fig. 3d) and a slightly less, but still non-negligible, twisting of 20° for the V-**BP** complex on Au(111) (Fig. 3a and b). This twisting of the ligand when complexed with V will cause the molecule to no longer be parallel with the underlying surface. It has been shown previously that a parallel molecular adsorbate orientation can optimize intermolecular and adsorbate-surface interactions and thus increase long range order [43]. It is therefore likely that the non-parallel orientation of **BP** in V-**BP** complexes limits long-range ordering of the complexes and leads to small, mobile units on the surface, preventing observation with STM. We note that this mobility was not observed in the case of V complexation with the larger **DPTZ** ligand.

Implementing simple changes in the design of the redox-active ligand can allow for higher oxidation of the single-site metal center. In the case of **BMTZ**, the addition of a tetrazine core with adjacent pyrimidine rings increases the electron storage of the ligand. **BMTZ** was used as a control ligand in these studies, as the redox-capabilities of the ligand have previously been published [10]. In those studies, upon exposure of **BMTZ** to metallic V and annealing to 170 °C, the V $2p_{3/2}$ peak position shifts to a higher BE (514.7 eV) consistent with a V(III) species.

The odd number oxidation state of V is attributed to a two-electron reduction of the tetrazine core and a delocalizing of an additional electron in the pyrimidine rings. Studies presented here looking at V-**BMTZ** on Au(111) demonstrate that the redox character observed is based on the organic ligand and target metal. As with the V-**BMTZ** on Au (100), the same shift in V $2p_{3/2}$ BE (514.8 eV) is observed upon vanadium's complexation with **BMTZ** and subsequent annealing to 170 °C on Au(111), shown in Fig. 1. Nitrogen 1*s* data is also consistent with previously reported studies where the 1:2:1 area ratio is observed [10], shown in Fig. 4. STM results of the V-**BMTZ** chains on Au(111) (Figure S3) do not show the characteristic chain growth at 45 ± 5° as observed on the Au(100) surface.

The coordination environment of the metal atom can further be modified to increase the single-site oxidation through the addition of two acidic protons, yielding **BIM** (Scheme 1), which has the highest

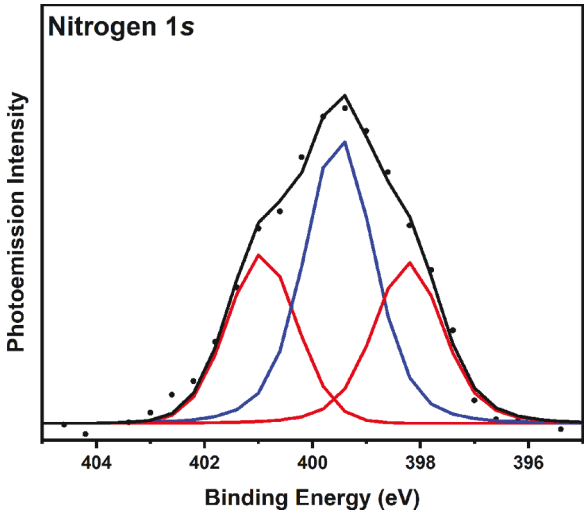

Fig. 4. XP Spectra of N 1*s* of V-**BMTZ** on Au(111). The observed 1:2:1 fitting of the N 1*s* curve matches previously reported studies.[10] The three features can be attributed to the reduction of the tetrazine core and partial reduction of the pyrimidine rings.

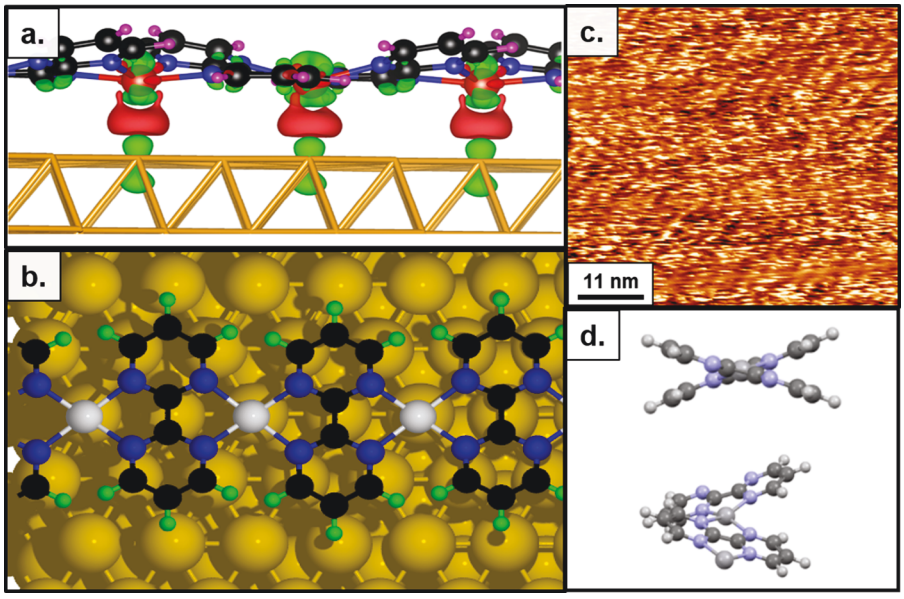

Fig. 3. V-**BP** on Au(111). (a) Side view showing calculated charge transfer of V-**BP** chains into the Au surface (charge accumulation and depletion are indicated in red and green, respectively), as well as a similar twist of the ligand when complexed with V. (b) Top view of the DFT-calculated structure. (c) STM image of V-**BP** on Au(111). The lack of surface structure is indicative of no long-range ordering of the V-**BP** on Au(111). (d) DFT structure of gaseous V-**BP** demonstrating the 32° twist of the **BP** ligand when complexed with V.

oxidizing capabilities of the ligands reported here. The addition of two acidic protons allows the ligand to undergo a non-reversible two electron reduction. An additional two electrons are able to be stored in the aromatic core of the ligand. These additional ligand design modifications give **BIM** a superior oxidizing capability over **BP**, even though the two ligands are similar in size.

Nitrogen 1*s* XP spectra of the free ligand on Au(111) shows that upon deposition onto the surface two distinct regions are observed corresponding to the pyrrolic and iminic nitrogen species at binding energies of 400.1 and 398.5 eV, respectively [44], as shown in Fig. 5. At ratios of 1:1 V:**BIM**, a decrease of the higher binding energy pyrrolic peak is observed suggesting that upon complexation with metallic V, some of the acidic protons are lost and would likely combine with other free protons and leave as gaseous H_2. The existence of a smaller pyrrolic peak indicates that some of the **BIM** remains protonated upon complexation with V. See Supporting Information, Figure S1, for additional fitting models with different ratios of pryollic to iminic nitrogen species for the 1:1 V-**BIM** complex. When increasing the ratio of V:**BIM** to 2:1 the N 1*s* FWHM decreases to 1.6 eV and becomes consistent with one type of nitrogen species. This single component N 1*s* XP spectra is fit with a binding energy of 398.8 eV, which is attributed to the iminic nitrogen. The complete loss of the pyrrolic component is evidence that **BIM** has been completely deprotonated (bottom right of Scheme 1). The removal of the two acidic protons upon complexation with a metal has been demonstrated with a variety of on-surface tetraphenylporphyrin complexes on a variety of surfaces [45–48]. The iminic nitrogen peak also shifts to a higher BE (399.0 eV) after loss of the acidic protons; similar observations have been observed with porphyrin species [44, 49–51].

STM imaging reveals a significant difference in V-**BIM** structure on Au(111) for the low (Fig. 6a and b) and high (Fig. 6c and d) metal:ligand ratios, which provides additional evidence for a change in the complexation of V-**BIM** at the different metal to ligand ratios, consistent with the deprotonation of **BIM**. The free ligand **BIM** is shown to form dense islands with molecules ordered in chains, as shown in Fig. S4. The observed chain structure for the 1:1 V:**BIM** system is shown for two surface coverages of 0.4 ML (Fig. 6a) and 0.9 ML (Fig. 6b). One significant difference between the free ligand and the 1:1 complexed ligand is the molecule-molecule spacing after complexation increases to 0.95 ± 0.05 nm. Interestingly, at the lower coverage (0.4 ML), the chains form

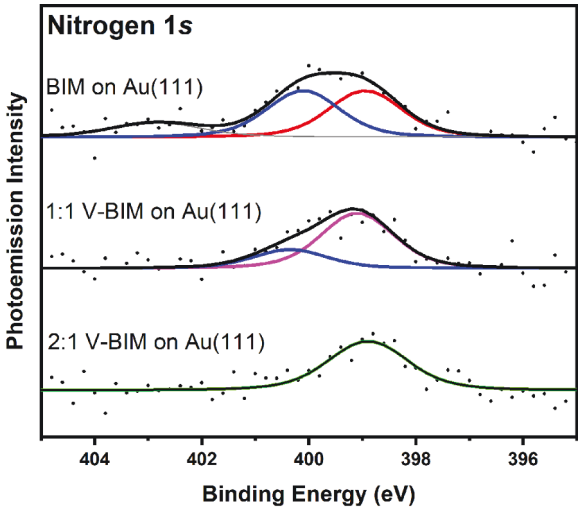

Fig. 5. XP spectra of N 1*s* of **BIM** on Au(111) before and after complexation with V metal. N 1*s* spectra of **BIM** (top) shows two different nitrogen species, attributed to pyrrolic (400.1 eV) and iminic (398.5 eV) nitrogen. At ratios of 1:1 V:**BIM** (middle) the pyrrolic feature diminishes due to the partial deprotonation of the acidic protons. At ratios of 2:1 V:**BIM** (bottom) the N 1*s* peak is consistent with a single species of nitrogen present, indicating complete deprotonation of the **BIM** molecule.

in pairs which can be attributed to an intermolecular interaction between the chains, and the measured distance between chains is 1.26 ± 0.03 nm (Fig. 6a). The lower coverage 1:1 V-**BIM** (Fig. 6e) pairs also are heavily influenced by the electronic reconstruction of the Au(111) substrate, with the distance between pairs measuring 6.3 ± 0.2 nm which is in good agreement with the reported spacing of the periodic parallel lines of the Au(111) reconstruction of 6.3 nm [52].

At the higher molecular coverage (0.9 ML), the spacing between the pairs disappears. Previous studies have shown that at higher molecule coverages the Au(111) reconstruction can be lifted [53, 54], which could potentially explain the disappearance of this spacing between the pairs. The chain to chain spacing also increases at the higher coverage to 1.49 ± 0.25 nm. Despite the lifting of the reconstruction row, the chains still remain straight and highly influenced by the underlying substrate and the chain growth direction remains consistent at 120°. At a V:**BIM** ratio of 2:1 (Fig. 6f), the observed surface structure is less influenced by the underlying Au substrate showing a loss of the three-fold symmetry for chain growth, shown in Fig. 6c and d.

XP spectra of the V 2*p* region indicate a notable oxidation state change of the V metal center upon complexation with **BIM** (Fig. 1), as for the other ligands, however, this spectrum has a significantly wider FWHM for V than with the other ligands studied. At a 1:1 V-**BIM** ratio the main feature of the V $2p_{3/2}$ peak is at 516.5 eV (Figure S2), which we assign as V(IV) (see discussion in Supporting information). There is also a component that is at a lower binding energy and corresponds to a lower oxidation state of V on the surface. When the V content on the surface is increased to a 2:1 ratio with **BIM**, there is a significant growth of the lower oxidation state peak (Figure S2), which is at a position consistent with V(0), *i.e.*, there may be excess non-complexed V on the surface, which would account for the nanoparticles observed in the STM images (Fig. 6).

5. Conclusion

In the work reported here we have demonstrated the ability to tune the oxidation state of single-site metal centers through rationale ligand design. Using the N-heterocyclic ligands of **BP, BMTZ,** and **BIM** complexed with metallic V, we have shown through monitoring of the binding energy of the metal center with XPS that the oxidation state of the V metal centers can be tuned from V(II) for **BP**, V(III) for **BMTZ**, and V(IV) for **BIM**. These redox-active ligands provide a similar coordination environments when complexed into one dimensional chains but result in different oxidation states for the single-site metal center. The three ligands are symmetrically similar and provide similar binding site geometries. We demonstrate that while providing assemblies of similar complexation structure, the three ligands differ drastically in terms of their potential for oxidizing an incoming zero-valent metal. We also highlight the importance of considering the resulting planarity of the metal ligand complexation for the development of long-range 2-D structures, as evidenced by our studies with **BP**. We see evidence of charge transfer in both the V 2*p* and N 1*s* peaks, but a lack of surface structure in STM due to a proposed twisting of the ligand. This lack of long-range order makes it more difficult to determine the uniformity of each individual metal center.

These studies of different redox-active ligands demonstrate how subtle changes in ligand design can have a large impact on controlling the oxidation state of the single-site metal center. Future ligand designs could incorporate acidic protons as a non-reversible reduction process if higher oxidation state metal-centers are desired. Studies of this type are important for developing understanding for next generation, highly efficient catalysts.

Author statement

Tobias W. Morris: STM and XPS experiments, investigation, formal analysis, Writing - Original Draft; David L. Wisman: STM and XPS

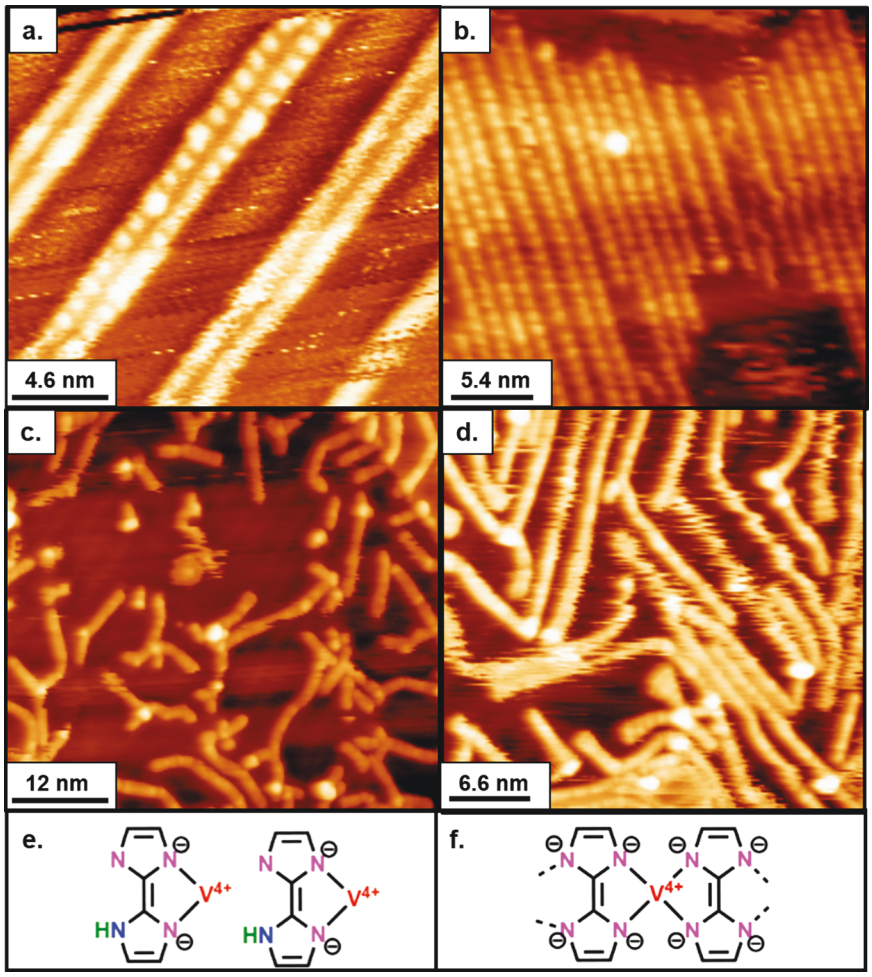

Fig. 6. (a) STM image of a 0.4 ML coverage of 1:1 V-**BIM** on Au(111) showing the formation of 1D chains in pairs illustrated in (e). The spacing of the pair matches the spacing of the Au(111) reconstruction, suggesting a strong surface interaction. (b) STM image of a 0.9 ML coverage of 1:1 V-**BIM** on Au(111) showing a similar chain structure as (a, e), but the spacing between pairs is diminished likely due to the lifting of the Au(111) reconstruction. (c) STM image of a 0.4 ML coverage of 2:1 V-**BIM** on Au(111) showing the formation of non-directional chains illustrated in (f) and (d) STM image of 0.8 ML coverage of 2:1 V-**BIM** on Au(111) showing a similar chain structure as the lower coverage species found in (c, f). The illustrations in (e, f) are based on the intermolecular spacing of the majority metal-ligand chain species on the surface. XPS indicates a second V minority species at lower oxidation state, which is likely related to the nanoparticles visible in the images.

experiments, investigation, formal analysis, Writing - Original Draft; Nassem U. Din: DFT calculations, formal analysis; Duy Le: DFT calculations, formal analysis; Talat S. Rahman: supervision, Writing - Review & Editing; Steven L Tait: supervision, conceptualization, project administration, Writing - Review & Editing;

Declaration of Competing Interest

The authors declare that they have no known competing financial interests or personal relationships that could have appeared to influence the work reported in this paper.

Acknowledgements

STM and XPS experiments were conducted at Indiana University (IU) and were supported by the National Science Foundation, CHE-1610984. DFT calculations were performed at the University of Central Florida with support from National Science Foundation, CHE-1955343, using computational resource from National Energy Research Scientific Computing Center (NERSC). D.L.W. acknowledges funding and support from the United States Department of Defense Naval Surface Warfare Center, Crane Division under the Naval Innovative Science and Engineering and Ph.D. fellowship programs. The authors wish to thank Professor Kenneth G. Caulton and I. Jake Huerfano for insightful discussions and Daniel Beagan for assistance with synthesis of BMTZ. On the occasion of this Virtual Special Issue, SLT gratefully acknowledges many vigorous discussions with Prof. Charles T. Campbell during his formative years as a Ph.D. student and ongoing support and mentorship in the years since.

Supplementary materials

Supplementary material associated with this article can be found, in the online version, at doi:10.1016/j.susc.2021.121888.

References

[1] X.-F. Yang, A. Wang, B. Qiao, J. Li, J. Liu, T. Zhang, Single-atom catalysts: a new frontier in heterogeneous catalysis, Acc. Chem. Res. 46 (2013) 1740–1748.
[2] H. Zhang, G. Liu, L. Shi, J. Ye, Single-atom catalysts: emerging multifunctional materials in heterogeneous catalysis, Adv. Energy Mater. 8 (2018), 1701343.
[3] A. Wang, J. Li, T. Zhang, Heterogeneous single-atom catalysis, Nat. Rev. Chem. 2 (2018) 65–81.
[4] Z. Kou, W. Zang, P. Wang, X. Li, J. Wang, Single atom catalysts: a surface heterocompound perspective, Nanoscale Horiz 5 (2020) 757–764.
[5] H. Jeong, S. Shin, H. Lee, Heterogeneous atomic catalysts overcoming the limitations of single-atom catalysts, ACS Nano 14 (2020) 14355–14374.
[6] L. Chen, I.S. Ali, G.E. Sterbinsky, J.T. Gamler, S.E. Skrabalak, S.L. Tait, Alkene hydrosilylation on oxide-supported pt-ligand single-site catalysts, ChemCatChem 11 (2019) 2843–2854.
[7] J. Liu, J. Shan, F.R. Lucci, S. Cao, E.C.H. Sykes, M. Flytzani-Stephanopoulos, Palladium–gold single atom alloy catalysts for liquid phase selective hydrogenation of 1-hexyne, Catal. Sci. Technol. 7 (2017) 4276–4284.
[8] X. Zhou, L. Chen, G.E. Sterbinsky, D. Mukherjee, R.R. Unocic, S.L. Tait, Pt-Ligand single-atom catalysts: tuning activity by oxide support defect density, Catal. Sci. Technol. 10 (2020) 3353–3365.
[9] D. Skomski, C.D. Tempas, G.S. Bukowski, K.A. Smith, S.L. Tait, Redox-active on-surface polymerization of single-site divalent cations from pure metals by a ketone-functionalized phenanthroline, J. Chem. Phys. 142 (2015), 101913.
[10] D. Skomski, C.D. Tempas, B.J. Cook, A.V. Polezhaev, K.A. Smith, K.G. Caulton, S. L. Tait, Two- and three- electron oxidation of single-site vanadium centers at surfaces by ligand design, J. Am. Chem. Soc. 137 (2015) 7898–7902.

[11] D. Skomski, C.D. Tempas, K.A. Smith, S.L. Tait, Redox-active on-surface assembly of metal–organic chains with single-site Pt (II), J. Am. Chem. Soc. 136 (2014) 9862–9865.

[12] C.D. Tempas, D. Skomski, B.J. Cook, D. Le, K.A. Smith, T.S. Rahman, K.G. Caulton, S.L. Tait, Redox isomeric surface structures are preferred over odd-electron Pt1+, Chem. Eur. J. 24 (2018) 15852–15858.

[13] T.W. Morris, I. Huerfano, M. Wang, D.L. Wisman, A.C. Cabelof, N.U. Din, C. D. Tempas, D. Le, A.V. Polezhaev, T.S. Rahman, Multi-electron reduction capacity and multiple binding pockets in metal–organic redox assembly at surfaces, Chem. Eur. J. 25 (2019) 5565–5573.

[14] P.V. Bonnesen, C.L. Puckett, R.V. Honeychuck, W.H. Hersh, Catalysis of Diels-Alder reactions by low oxidation state transition-metal Lewis acids: fact and fiction, J. Am. Chem. Soc. 111 (1989) 6070–6081.

[15] D.G. McCollum, G.P. Yap, L. Liable-Sands, A.L. Rheingold, B. Bosnich, Bimetallic Reactivity, Oxo transfer reactions with a heterobimetallic complex of Iron (II) and Vanadium (III), Inorg. Chem. 36 (1997) 2230–2235.

[16] K. Weber, E.M. Schnöckelborg, R. Wolf, Catalytic Properties of Low Oxidation State Iron Complexes in Cross-Coupling Reactions: Anthracene Iron (− I) Complexes as Competent Catalysts, ChemCatChem 3 (2011) 1572–1577.

[17] K.G. Caulton, Systematics and future projections concerning redox-noninnocent amide/imine ligands, Eur. J. Inorg. Chem. 2012 (2012) 435–443.

[18] S.L. Tait, Y. Wang, G. Costantini, N. Lin, A. Baraldi, F. Esch, L. Petaccia, S. Lizzit, K. Kern, Metal-organic coordination interactions in Fe-Terephthalic acid networks on Cu(100), J. Am. Chem. Soc. 130 (2008) 2108–2113.

[19] E. Amadio, R. Di Lorenzo, C. Zonta, G. Licini, Vanadium catalyzed aerobic carbon-carbon cleavage, Coord. Chem. Rev. 301 (2015) 147–162.

[20] T. Andrushkevich, V. Kaichev, Y.A. Chesalov, A. Saraev, V. Buktiyarov, Selective oxidation of ethanol over vanadia-based catalysts: The influence of support material and reaction mechanism, Catal. Today 279 (2017) 95–106.

[21] C. Bolm, F. Bienewald, Asymmetric sulfide oxidation with vanadium catalysts and H2O2, Angew. Chem. Int. Ed. 34 (1996) 2640–2642.

[22] S. Guimond, M.A. Haija, S. Kaya, J. Lu, J. Weissenrieder, S. Shaikhutdinov, H. Kuhlenbeck, H.-J. Freund, J. Döbler, J. Sauer, Vanadium oxide surfaces and supported vanadium oxide nanoparticles, Top. Catal. 38 (2006) 117–125.

[23] R.R. Langeslay, D.M. Kaphan, C.L. Marshall, P.C. Stair, A.P. Sattelberger, M. Delferro, Catalytic applications of vanadium: a mechanistic perspective, Chem. Rev. 119 (2018) 2128–2191.

[24] G. Licini, V. Conte, A. Coletti, M. Mba, C. Zonta, Recent advances in vanadium catalyzed oxygen transfer reactions, Coord. Chem. Rev. 255 (2011) 2345–2357.

[25] I. Muylaert, P. Van Der Voort, Supported vanadium oxide in heterogeneous catalysis: elucidating the structure–activity relationship with spectroscopy, PCCP 11 (2009) 2826–2832.

[26] I.E. Wachs, Catalysis science of supported vanadium oxide catalysts, Dalton Trans 42 (2013) 11762–11769.

[27] J.P. Ibe, P.P.B. Jr., S.L. Brandow, R.A. Brizzolara, N.A. Burnham, D.P. DiLella, K. P. Lee, C.R.K. Marrian, R.J. Colton, On the electrochemical etching of tips for scanning tunneling microscopy, J. Vac. Sci. Technol., A 8 (1990) 3570–3575.

[28] J.E. McKendry, C.S. Allen, K. Critchley, M.Ł. Górzny, A.S. Walton, S.D. Evans, Magnetic field enhanced nano-tip fabrication for four-probe STM studies, Nanotechnol 19 (2008), 085201.

[29] I. Horcas, R. Fernández, J.M. Gómez-Rodríguez, J. Colchero, J. Gómez-Herrero, A. M. Baro, WSXM: A software for scanning probe microscopy and a tool for nanotechnology, Rev. Sci. Instrum. 78 (2007), 013705 (013701–013709).

[30] S. Stepanow, T. Strunskus, M. Lingenfelder, A. Dmitriev, H. Spillmann, N. Lin, J. V. Barth, C. Wöll, K. Kern, Deprotonation-Driven Phase Transformations in Terephthalic Acid Self-Assembly on Cu(100), J. Phys. Chem. B 108 (2004) 19392–19397.

[31] Y. Ge, H. Adler, A. Theertham, L.L. Kesmodel, S.L. Tait, Adsorption and bonding of first layer and bilayer Terephthalic Acid on the Cu(100) Surface by High-Resolution Electron Energy Loss Spectroscopy, Langmuir 26 (2010) 16325–16329.

[32] G. Kresse, J. Furthmuller, Efficiency of ab-initio total energy calculations for metals and semiconductors using a plane-wave basis set, Computational Materials Science 6 (1996) 15–50.

[33] G. Kresse, D. Joubert, From ultrasoft pseudopotentials to the projector augmented-wave method, Phys. Rev. B: Condens. Matter 59 (1999) 1758–1775.

[34] J.P. Perdew, K. Burke, M. Ernzerhof, Generalized Gradient Approximation Made Simple, Phys. Rev. Lett. 77 (1996) 3865–3868.

[35] S. Grimme, J. Antony, S. Ehrlich, H. Krieg, A consistent and accurate ab initio parametrization of density functional dispersion correction (DFT-D) for the 94 elements H-Pu, J. Chem. Phys. 132 (2010), 154104.

[36] L. Artiglia, S. Agnoli, G. Granozzi, Vanadium oxide nanostructures on another oxide: The viewpoint from model catalysts studies, Coord. Chem. Rev. 301 (2015) 106–122.

[37] S. Beke, A review of the growth of V2O5 films from 1885 to 2010, Thin Solid Films 519 (2011) 1761–1771.

[38] C.A. Carrero, R. Schloegl, I.E. Wachs, R. Schomaecker, Critical literature review of the kinetics for the oxidative dehydrogenation of propane over well-defined supported vanadium oxide catalysts, ACS Catal 4 (2014) 3357–3380.

[39] G.C. Bond, S.F. Tahir, Vanadium-oxide monolayer catalysts - preparation, characterization and catalytic activity, Appl. Catal. 71 (1991) 1–31.

[40] S. Surnev, G. Kresse, M.G. Ramsey, F.P. Netzer, Novel interface-mediated metastable oxide phases: Vanadium oxides on Pd(111), Phys. Rev. Lett. 87 (2001).

[41] C.D. Tempas, T.W. Morris, D.L. Wisman, D. Le, N.U. Din, C.G. Williams, M. Wang, A.V. Polezhaev, T.S. Rahman, K.G. Caulton, Redox-active ligand controlled selectivity of vanadium oxidation on Au (100), Chem. Sci. 9 (2018) 1674–1685.

[42] L. Jiang, B. Zhang, G. Médard, A.P. Seitsonen, F. Haag, F. Allegretti, J. Reichert, B. Kuster, J.V. Barth, A.C. Papageorgiou, N-Heterocyclic carbenes on close-packed coinage metal surfaces: bis-carbene metal adatom bonding scheme of monolayer films on Au, Ag and Cu, Chem. Sci. 8 (2017) 8301–8308.

[43] G. Conboy, H.J. Spencer, E. Angioni, A.L. Kanibolotsky, N.J. Findlay, S.J. Coles, C. Wilson, M.B. Pitak, C. Risko, V. Coropceanu, J.-L. Brédas, P.J. Skabara, To bend or not to bend – are heteroatom interactions within conjugated molecules effective in dictating conformation and planarity? Mater. Horiz. 3 (2016) 333–339.

[44] M. Chen, X. Feng, L. Zhang, H. Ju, Q. Xu, J. Zhu, J.M. Gottfried, K. Ibrahim, H. Qian, J. Wang, Direct synthesis of nickel (II) tetraphenylporphyrin and its interaction with a Au (111) surface: a comprehensive study, J. Phys. Chem. C 114 (2010) 9908–9916.

[45] W. Auwarter, A. Weber-Bargioni, S. Brink, A. Riemann, A. Schiffrin, M. Ruben, J. V. Barth, Controlled metalation of self-assembled porphyrin nanoarrays in two dimensions, ChemPhysChem 8 (2007) 250–254.

[46] C. Bürker, A. Franco-Cañellas, K. Broch, T.-L. Lee, A. Gerlach, F. Schreiber, Self-Metalation of 2 H-Tetraphenylporphyrin on Cu (111) Studied with XSW: Influence of the Central Metal Atom on the Adsorption Distance, J. Phys. Chem. C 118 (2014) 13659–13666.

[47] K. Diller, F. Klappenberger, M. Marschall, K. Hermann, A. Nefedov, C. Wöll, J. Barth, Self-metalation of 2H-tetraphenylporphyrin on Cu (111): An x-ray spectroscopy study, J. Chem. Phys. 136 (2012), 014705.

[48] M. Röckert, S. Ditze, M. Stark, J. Xiao, H.-P. Steinrück, H. Marbach, O. Lytken, Abrupt coverage-induced enhancement of the self-metalation of tetraphenylporphyrin with Cu (111), J. Phys. Chem. C 118 (2014) 1661–1667.

[49] F. Buchner, K. Flechtner, Y. Bai, E. Zillner, I. Kellner, H.-P. Steinrück, H. Marbach, J.M. Gottfried, Coordination of iron atoms by tetraphenylporphyrin monolayers and multilayers on Ag (111) and formation of iron-tetraphenylporphyrin, J. Phys. Chem. C 112 (2008) 15458–15465.

[50] J.M. Gottfried, Surface chemistry of porphyrins and phthalocyanines, Surf. Sci. Rep. 70 (2015) 259–379.

[51] J.M. Gottfried, K. Flechtner, A. Kretschmann, T. Lukasczyk, H.-P. Steinrück, Direct synthesis of a metalloporphyrin complex on a surface, J. Am. Chem. Soc. 128 (2006) 5644–5645.

[52] J. Barth, H. Brune, G. Ertl, R. Behm, Scanning tunneling microscopy observations on the reconstructed Au (111) surface: Atomic structure, long-range superstructure, rotational domains, and surface defects, Phys. Rev. B: Condens. Matter 42 (1990) 9307–9318.

[53] P. Maksymovych, D.C. Sorescu, J.T. Yates Jr, Gold-adatom-mediated bonding in self-assembled short-chain alkanethiolate species on the Au (111) surface, Phys. Rev. Lett. 97 (2006), 146103.

[54] A.D. Jewell, H.L. Tierney, E.C.H. Sykes, Gently lifting Gold's herringbone reconstruction: trimethylphosphine on Au (111), Phys. Rev. B: Condens. Matter 82 (2010), 205401.